

Spectral Variation of the Seyfert 1 Galaxy MCG-6-30-15 observed with Suzaku

Takehiro MIYAKAWA^{1,2}, Ken EBISAWA^{1,2}, Yuichi TERASHIMA³, Fuminori TSUCHIHASHI³, Hajime INOUE¹
and Piotr Życki⁴

¹*The Institute of Space and Astronautical Science (ISAS), Japan Aerospace Exploration Agency (JAXA),
3-1-1 Yoshinodai, Sagamihara, Kanagawa 229-8510*

²*Department of Astronomy, Graduate School of Science, the University of Tokyo,
7-3-1 Hongo, Bunkyo-ku, Tokyo 113-0033*

³*Department of Physics, Ehime University, 2-5 Bunkyocho, Matsuyama, Ehime 790-8577*

⁴*Nicolaus Copernicus Astronomical Center, Bartycza, 18, Warsaw, Poland
miyakawa@astro.isas.jaxa.jp*

(Received (2009 June 16); accepted (2009))

Abstract

We have investigated spectral variation of the Seyfert 1 galaxy MCG-6-30-15 observed with Suzaku in January 2006 for three separate periods spreading over fourteen days. We found that the time-averaged continuum energy spectrum between 1 keV and 40 keV can be approximated with a spectral model composed of the direct power-law component, its reflection component, two warm absorbers with different ionization states, and neutral absorption. We have taken two approaches to study its spectral variation at various timescales: The first approach is to make intensity-sliced spectra and study correlation between the intensity and spectral shape. The second approach is to study spectral changes between the intervals when the source flux is above (“bright state”) and below (“faint state”) the average for fixed time-intervals. In both approaches, we found a clear correlation between the intensity in the 6 – 10 keV band and the spectral ratio of 0.5 – 3.0 keV/6.0– 10 keV. Such a spectral variation requires change of the apparent slope of the direct component, whereas the shape and intensity of the reflection component being invariable. The observed apparent spectral change is explained by variation of the ionization degree of one of the two warm absorbers due to intrinsic source luminosity variation. Current results suggest that the warm absorber has a critical role to explain the observed continuum spectral shape and variation of MCG-6-30-15, which is essential to constrain parameters of the putatively broadened iron line emission feature.

Key words: galaxies: active – galaxies: individual (MCG-6-30-15) – galaxies: Seyfert – X-rays: galaxies

1. Introduction

The Seyfert 1 galaxy MCG-6-30-15 has been extensively studied with ASCA (Iwasawa et al. 1996,1999; Matsumoto et al. 2003), BeppoSAX (Guainazzi et al. 1999), Rossi X-ray Timing Explorer (Lee et al. 1999, Vaughan & Edelson 2001), Chandra (Lee et al. 2001, Young et al. 2005, Gibson et al. 2007), XMM-Newton (Fabian et al. 2002, Vaughan & Fabian 2004, Ponti et al. 2004), Suzaku (Miniutti et al. 2007), and a combination of Suzaku, Chandra and XMM-Newton (Miller, Turner, and Reeves 2008). ASCA discovered a broad and skewed emission line feature around 5–7 keV in the spectrum of MCG-6-30-15 for the first time (Tanaka et al. 1995). The iron line is emitted as a part of the reflection spectrum from the accretion disk, irradiated by a primary continuum of the central engine. Fabian et al. (1989) suggested that the iron line due to disk reflection is in general broadened and skewed by the Doppler effects and gravitational redshift if the line is emitted in the vicinity of the black hole. In fact, the iron line profile observed with ASCA is well explained with such a “disk-line” model (Tanaka et

al. 1995).

Meanwhile, Fabian et al. (2002) and Matsumoto et al. (2003) reported significant *invariability* in the iron line energy band of MCG 6-30-15 in XMM-Newton and ASCA observations, respectively. Inoue and Matsumoto (2003) pointed out that the absorbed spectrum due to photoionized warm absorbers mimics the shape of the strongly redshifted iron line, and that variation of the warm absorbers may explain such invariability in the iron line region. On the other hand, Miniutti and Fabian (2004) proposed that the observed invariability of the iron line may be explained if the disk reflection and line photon production takes place very close to the black hole, such that the apparent invariability of the iron line is due to general relativistic light-bending effects. In fact, Miniutti et al. (2007) claim that the strong reflection, the broad iron line and invariability of the iron line observed with Suzaku may be explained with the light-bending model, and suggest that the innermost disk radius extends down to about as low as two gravitational radii. Meanwhile, Niedźwiecki & Życki (2008) independently re-examined the light-bending model and concluded that it is indeed possible that a re-

flected component is very weakly variable compared to the primary emission, if a source is moving *radially* very close to the rotating black hole, while whether such a particular movement is plausible or not is another question.

On the other hand, a similarly weakly variable, *apparently broad* Fe line in NGC 4151 is most likely to be an artifact of incorrect modelling of the absorbers, and the spectrum is in fact dominated by a narrow emission line (Ogle et al. 2000; de Rosa et al. 2007). As a matter of fact, Takahashi, Inoue, and Dotani (2002) confirmed, from a very long RXTE monitoring data, an unambiguous evidence that the reverberation of the iron line emission takes place not in the vicinity of the central black hole but very far from the black hole ($\sim 10^{17}$ cm). Therefore, at least in NGC 4151, most iron line photons are produced very far from the black hole and thus invariable on a timescale of $\sim 10^5$ sec.

In MCG-6-30-15 too, Young et al. (2005) reported a weak and narrow emission line at 6.4 keV, which indicates that some reflection does take place in a distant material, e.g., the narrow-line region or the pc-scale torus. However, equivalent width of the narrow line in MCG-6-30-15 (~ 18 eV) is much smaller than in NGC 4151 ($\lesssim 2$ keV; Takahashi, Inoue and Dotani 2002). Therefore, invariability of the apparently broadened iron line feature in MCG-6-30-15 has yet to be explained.

The question in MCG-6-30-15 is thus whether the Fe line is broad and its lack of variability is a result of the relativistic effect, or it is rather narrow, comes from a distant and extended medium, which would naturally smear the variability. The crucial element to address the problem is to model the underlying continuum spectrum and study its variation. The broad band continuum in MCG-6-30-15 is complex, with strong modification from warm absorbers (Reynolds et al. 1995, Otani et al. 1996, Lee et al. 2001, Sako et al. 2003, Turner et al. 2003, Turner et al. 2004, Young et al. 2005, Miller et al. 2008). Moreover, the continuum spectral shape is variable, and the spectral variation is suggested to be driven mostly by variations of the complex warm absorbers (Miller et al. 2008).

In this paper we attempt to comprehensively characterize the spectral variability of the source in a model independent manner as much as possible. We characterize spectral variations at different timescales, as well as at different source flux levels. We use Suzaku data taken in Jan 2006 (total exposure time is 339 ksec) for this purpose. Suzaku's broad energy coverage (0.6–40 keV), excellent spectral resolution and a large effective area, make it an ideal instrument to study spectral variation of moderately bright AGNs such as MCG-6-30-15. Our goal is to find a reasonable spectral model of MCG-6-30-15 which is able to explain the observed spectral variation at various timescales with minimum numbers of parameters, and to study effects of warm absorbers. Such a reasonable spectral model is very needed to disentangle the tough disk-line problem, since the broad iron line feature is affected by the choice of continuum spectral models.

2. Observation and Data Reduction

The Suzaku satellite (Mitsuda et al. 2007) has observed MCG-6-30-15 ($z = 0.00775$; Fisher et al. 1995) four times. The first observation was performed between August 17–19 in 2005 for about 45 ksec. In 2006 January, the source was observed three times, between 9–14 (143 ksec exposure), 23–26 (99 ksec), and 27–30 (97 ksec). In this paper, we use the data taken in 2006 January.

For data reduction we used the HEADAS 6.5 software package, provided by NASA/GSFC. The XIS data were screened with XSELECT using the standard criterion (Koyama et al. 2007). The XIS spectra and light-curves were extracted from circular regions of 3.82 arcmin radius centred on the source, while background products were extracted from the outer annulus region with a total area being equal to that of the source region.

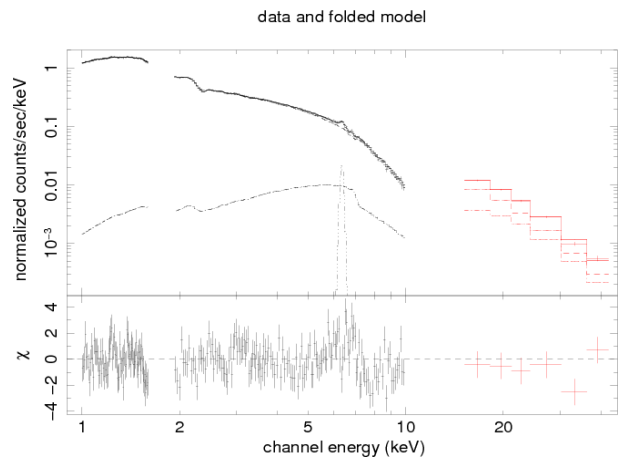


Fig. 1. Spectral fit result for the time-averaged XIS and PIN spectra (1–40 keV) with a *narrow* iron emission line (intrinsic line width is fixed to $1 \sigma = 10$ eV).

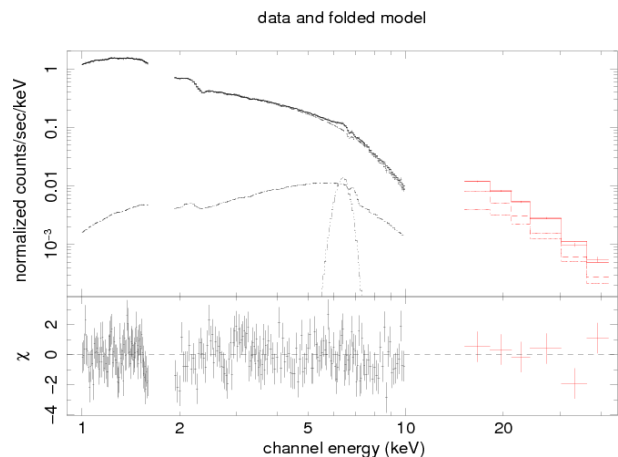


Fig. 2. Spectral fit result for the time-averaged XIS and PIN spectra (1–40 keV) with a *broad* iron emission line (intrinsic line width is allowed to be free and $1 \sigma = 290$ eV).

We generated XIS response matrices using the `xisrmfgen` software, which takes into account the time-variation of the energy response. As for generating ancillary response files (ARFs), we used `xissimarfgen` (Ishisaki et al. 2007). This tool calculates ARFs through ray-tracing, and we selected the number of input photons as 400000, with the “estepfile” parameter “full”.

After extracting the products for the back-illuminated CCD (XIS1) and for the three front-illuminated CCD XIS detectors (XIS0, XIS2, XIS3) separately, we found the XIS0, XIS2, and XIS3 products are almost identical to each other. So we combined the XIS0, XIS2, and XIS3 products in our analysis. We used the `addascaspec` to combine the XIS spectra and responses.

As for HXD/PIN (Takahashi et al. 2007), instrumental background model is provided by the HXD instrument team in the form of simulated PIN event files. These background event files do not contain the cosmic X-ray background (CXB) component, which we estimated separately using the PIN response for flat emission distribution (`ae_hxd_pinflate1_20080129.rsp`) assuming the CXB spectrum measured by HEAO-1 (Boldt 1987).

3. Data Analysis and Results

3.1. Spectral Fitting for the Average Spectrum

First, in this section, we study the time-average spectrum of MCG-6-30-15 to find a physically plausible spectral model. Then, in the following sections, we will use the same spectral model to see which parameters are variable to explain the observed spectral variation (sections 3.2 and 3.3). The spectral model we adopt is the following; (1) power-law with an exponential cut-off, (2) disk reflection component from neutral matter (“pexrav”; Magdziarz & Zdziarski 1995), (3) iron emission line, (4) two warm absorbers with different ionization states, and (5) neutral photoelectric absorption (“phabs”; Balucinska-Church & McCammon 1992). (6) a narrow gaussian absorption line to account for the instrumental feature around the Au M-edge.

We use XSTAR Version 2.1kn8 (Kallman et al. 2004; see also the note in the end of the paper) to model the warm absorbers, assuming the solar abundance and the photon index of the ionizing spectrum 2.0. The temperature, pressure and density of the warm absorbers are assumed to be 10^5 K, 0.03 dyne/cm² and 10^{12} cm⁻³, respectively. We made a grid model by running XSTAR for different values of ξ and N_H ; the log ξ values are from 0.1 to 5 (erg cm s⁻¹) and N_H values are from 10^{20} to 10^{24} (cm⁻²). The number of steps for log ξ and N_H are both 20, thus our grid model has 20×20 grid-points.

All the fits were made with XSPEC v11 (Arnaud 1996). In Fig.1, we show the fitting result for total average spectrum with a *narrow* emission line (line width is fixed at $1\sigma = 10$ eV), where reduced chisq is 1.51 ($\chi^2/\text{d.o.f} = 339.3/224$). The broadband 1–40 keV spectrum was fitted reasonably well, while there remain some residuals in the energy range of 5–7 keV (within $\pm 5\%$) for putatively broad iron emission line. Note that the XSTAR

warm absorber model includes the absorption lines, and in fact the observed FeXXV and FeXXVI absorption line features at 6.67 keV and 6.97 keV are successfully modeled. However, we found this spectral model fails to fit the data below 1 keV; this issue is discussed separately in section 3.4.

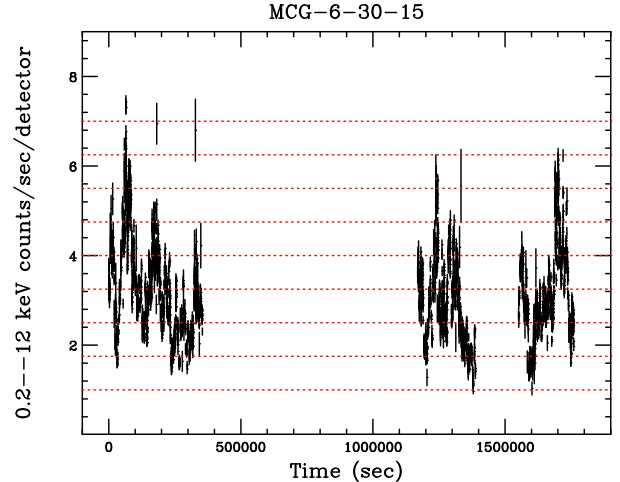


Fig. 3. 0.2–12 keV XIS light curve of the 2006 observation. The count rate intervals with which intensity-sliced spectra are made are also indicated.

If we allow the intrinsic line width to be free, the fit significantly improved, where reduced chisq is 1.20 ($\chi^2/\text{d.o.f} = 267.4/222$). Central energy of the line is 6.42 ± 0.06 keV, and the width is $1\sigma = 290 \pm 60$ eV (Figure 2). The equivalent width is 100 ± 20 eV. In Fig.2, we show the fitting result for the total average spectrum with a broad line. Note that our model does not require an extremely broadened iron emission line, which may be expected from very vicinity of a fast rotating black hole. The best-fit parameters are shown in Table1.

3.2. Spectral Variation

Next, we study spectral variation of the source in a model-independent manner. First, we make “intensity-sliced energy spectra” as follows:

- 1) Create a light curve (the average of XIS0, XIS2, and XIS3), with a bin-width of 128 sec in the 0.2 – 12 keV band. We found that the count rate varies from ~ 1 to ~ 7 cts/sec. Figure3 shows the 0.2–12 keV XIS light curve used in the present data analysis.
- 2) Choose time periods when the source intensity is in the ranges of 1–1.75, 1.75–2.50, 2.50–3.25, 3.25–4.00, 4.00–4.75, 4.75–5.50, 5.50–6.25, 6.25–7.00 cts/sec. These intensity ranges are chosen so that the exposure times for individual intensity bins are approximately equal.
- 3) From the eight intervals corresponding to the different source flux levels, we create eight intensity-sliced energy spectra (the sum of XIS0, XIS2, and XIS3).

Second, to study spectral variations in various timescales, we extract “bright spectra” and “faint spectra” as follows:

Table 1. Results of the average spectral fitting in 1–40 keV*

	broad line	narrow line
N_H (10^{21} cm $^{-2}$)	2.2 ± 0.2	1.7 ± 0.2
N_H (10^{22} cm $^{-2}$)	6^{+3}_{-2}	10^{+6}_{-4}
$\log \xi$	3.3 ± 0.1	3.6 ± 0.2
N_H (10^{21} cm $^{-2}$)	2.4 ± 0.8	1.5 ± 0.4
$\log \xi$	$1.7^{+0.1}_{-0.3}$	$1.0^{+0.2}_{-0.4}$
Line E (keV)	6.42 ± 0.06	6.35 (fix)
sigma (keV)	0.29 ± 0.06	0.01 (fix)
norm (10^{-5})	4.4 ± 0.7	1.7 ± 0.3
EW (eV)	100 ± 20	38 ± 6
cutoffpl K (10^{-2})	1.47 ± 0.05	1.38 ± 0.03
photon index	1.95 ± 0.02	1.90 ± 0.02
E_{cut} (keV)	160 (fix)	160 (fix)
cosIncl	0.866 (fix)	0.866 (fix)
$\Omega/2\pi$	1.0 ± 0.2	0.8 ± 0.2
Line E (keV)	2.35 ± 0.02	2.35 ± 0.02
sigma (keV)	0.01 (fix)	0.01 (fix)
norm (10^{-5})	-2.2 ± 0.5	-2.2 ± 0.5
reduced chisq (d.o.f)	1.20 (222)	1.51 (224)

* Errors are quoted at statistical 90% level. Constant factor to adjust normalizations between XIS and PIN is 1:1.086 (Ishida, Suzuki, and Someya 2007). Units of the cutoff power-law and pexrav normalization are photons/s/cm 2 /keV at 1 keV. Ω is solid angle of the reflector seen from the central source, and $\Omega/2\pi$ is defined as the ratio of the normalization of the reflection component to that of the cutoff power-law component. Unit of the line normalization is photons/s/cm 2 . Redshift of warm absorber and objects are 0.001 and 0.00775, respectively (Young et al. 2005, Fisher et al. 1995). Energy cutoff (E_{cut}) is fixed to 160 keV (Guainazzi et al. 1999). The solar abundances are defined in Greeves, Noels and Sauval (1996) for the warm absorbers and in Anders & Ebihara (1982) for the reflection component (pexrav).

- 1) Divide the entire observation period into a series of the time-interval of which length is T .
- 2) Create light curves for individual intervals with a time-bin-width of 128 sec, and calculate the average count rate for each interval T .
- 3) For each interval, create the “bright spectrum” from the period when the XIS count rates (0.2 – 12 keV) are higher than the average, and the “faint spectrum” when the count rates are lower than the average.
- 4) Average the bright spectra and faint spectra for all the intervals.
- 5) Thus, for a given T , we have one bright spectrum and one faint spectrum.
- 6) Repeat the procedure for different time-intervals of T . As for T , we chose 5,000, 9,000, 15,000, 40,000, 75,000 and 200,000 sec.

Thus, we have six “bright spectra” and six “faint spectra” corresponding to these timescales. Note that there are data gaps within a single time interval, since Suzaku has a low-earth orbit and the observation is intermittent every $\sim 3,000$ seconds or so. Typical exposure is $\sim 50\%$ of the bin-size.

From the eight intensity-sliced spectra, six bright spectra and six faint spectra thus created, we studied spectral variations in a model independent manner by calculating

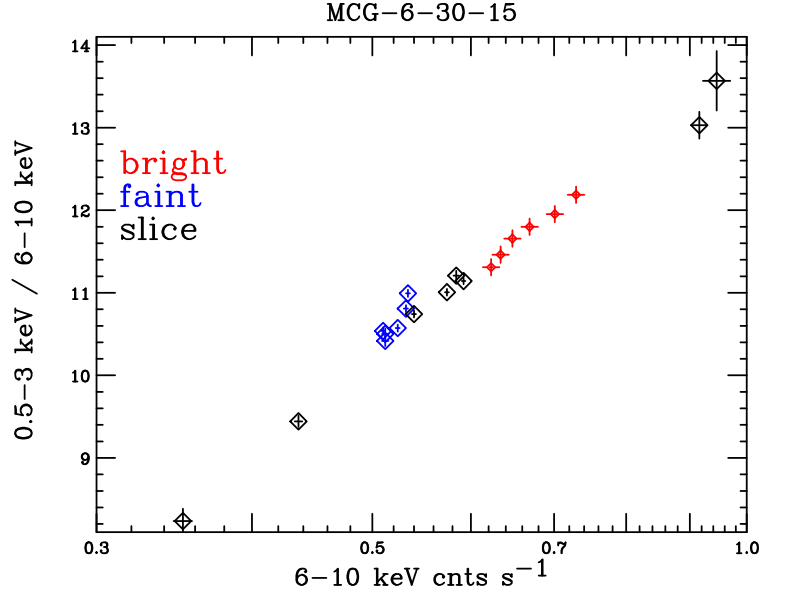


Fig. 4. Correlation between the flux in 6.0–10 keV and the hardness ratio of 0.5–3.0 keV/6.0–10 keV for the “intensity-sliced spectra” (black), “bright spectra” (red) and “faint spectra” (blue).

spectral hardness ratios between different energy bands. Consequently, we discovered a significant correlation between the intensity in the 6.0 – 10 keV and the spectral ratio of 0.5 – 3.0 keV / 6.0 – 10 keV. This correlation is shown in Figure 4.

Figure 5 gives the 6.0 – 10 keV intensity and the 0.5 – 3.0 / 6.0 – 10 keV spectral-ratio as functions of the time-interval T . From these figures, it is obvious that the intensity and spectral variations are more prominent with increasing timescales. In fact, Figure 6 shows ratios of the bright spectra to the faint spectra for different time-intervals. It is obvious that the “bright” spectra are steeper than the “dim” spectra below ~ 10 keV for all the time scales, and that the spectral difference becomes more significant with increasing timescales. We emphasize that the spectral variation we found here is *model independent*.

3.3. Spectral Fitting for the Bright and Faint State Spectra

Next, we quantify the observed spectral variation on different timescales using the same model as for the average spectrum. We try to fit the six “bright” spectra and the six “faint” spectra simultaneously (both XIS and PIN in 1 – 40 keV) with minimum numbers of variable parameters. As a result, we found that the twelve spectra are fitted reasonably well with keeping the reflection component constant, and only varying normalization of the direct component and another parameter to describe its apparent spectral slope, such that the direct component spectrum steepens as the flux increases (Figures 4 and 6). Namely, we found *only two parameters are required* to describe continuum spectral variations of the twelve

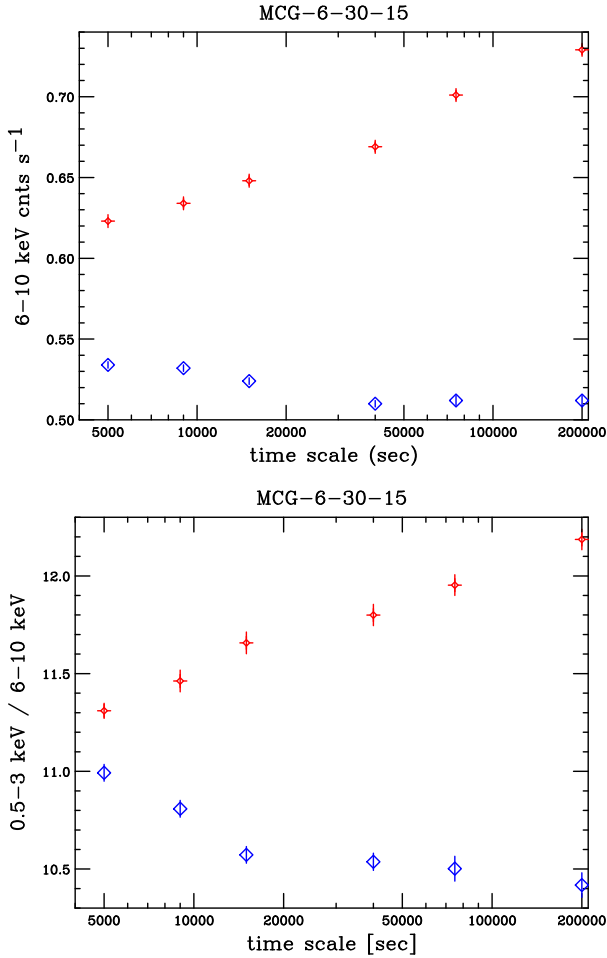


Fig. 5. The 6.0 – 10 keV intensity (top) and the spectral hardness ratio (bottom) of the bright (red) and faint (blue) spectra as functions of the time-intervals, T .

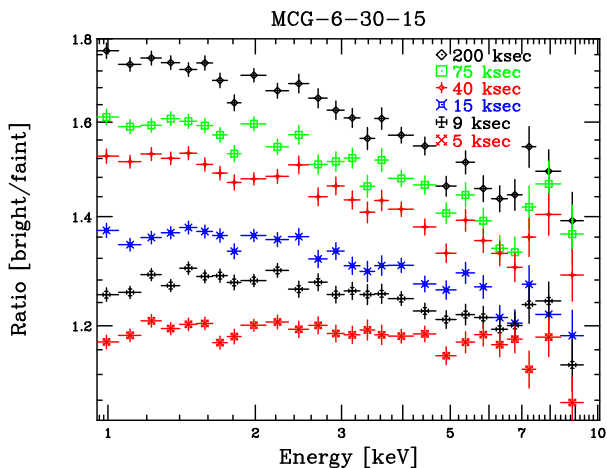


Fig. 6. Spectral ratios of the bright spectra to the faint spectra for six different timescales.

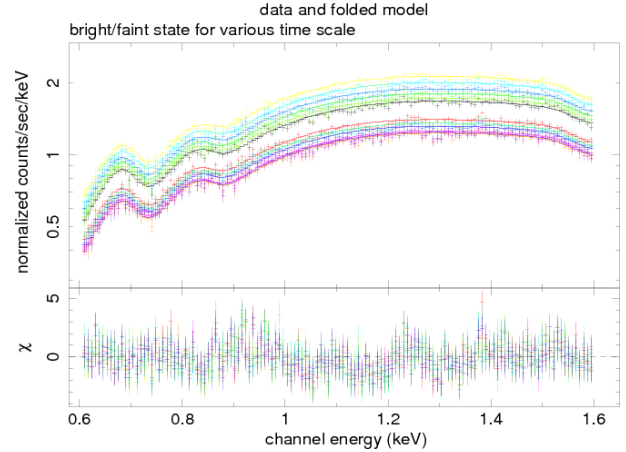


Fig. 7. Simultaneous fit in the 0.6–1.6 keV band for the twelve spectra (bright and faint spectra for the 6 timescales) with a power-law plus two absorption edge model.

data-sets, whereas all the other spectral parameters are constant (iron line flux is slightly variable, which hardly affects the overall spectral shape). We found that either power-law photon index, ionization parameter or column density of the lower-ionized warm absorber almost equally reproduces the observed spectral change of the direct component. The best-fit parameters are shown in Table 2 for the twelve spectra, when the power-law index, the ionization parameter and the column density is varied, respectively, besides the power-law normalization.

3.4. Spectral Variation below 1 keV

We found our two warm-absorber model fails to explain the energy spectra below 1 keV. Lee et al. (2001) reported strong oxygen absorption lines using Chandra grating observation, which suggests there is another warm absorber component responsible for the oxygen features below 1 keV. In any case, our aim is to explain and quantify the observed spectral variation with a simple model as much as possible, thus we fit the 0.6–1.6 keV spectra using a power-law component and two absorption edges to approximate the ionized oxygen edges and absorption lines. The twelve spectra are fitted simultaneously, as in the previous section.

The best-fit absorption edge energies are 0.706 keV and 0.855 keV, which are considered to be primarily due to absorption edges/lines of OVII and OVIII, respectively. We found that we can fit all the twelve spectra with common photon index and the 0.706 keV edge optical depth, while only the power-law normalization and the optical depth of the 0.855 keV edge are variable (Fig. 7). Reduced χ^2 was 1.30 ($\chi^2/\text{d.o.f} = 2077.7/1604$).

The best-fit parameters are shown in Table 3. We found that optical depth of the O VIII edge becomes deeper and shallower for the faint state and the bright state, respectively, as the variation timescale increases (bottom panel in Fig. 8). This result suggests that the ionization degree of the warm absorber is varying, since the oxygen is considered to be more highly ionized and the OVIII

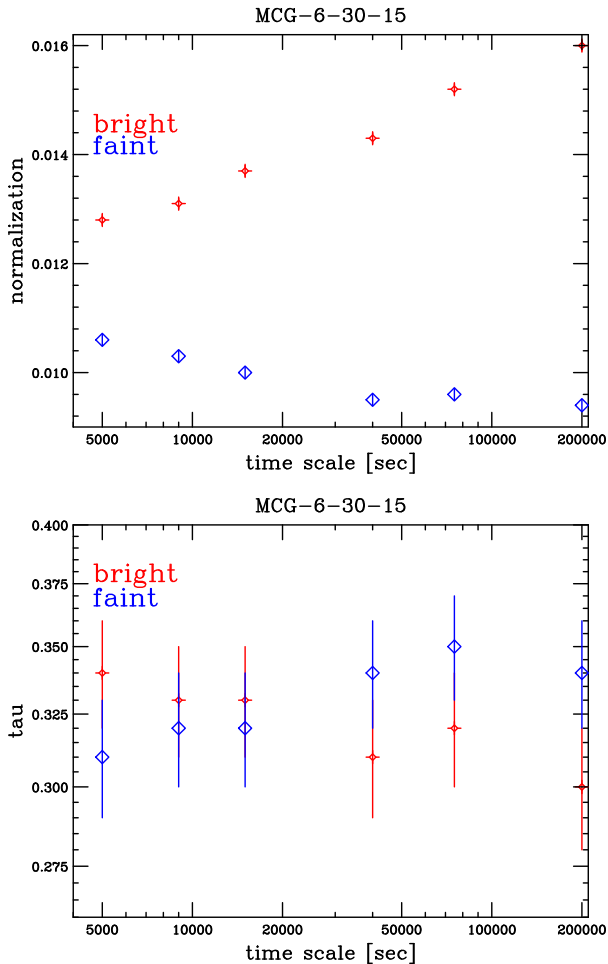


Fig. 8. Variation of the power-law normalization and depth of the OVIII edge to describe the spectral variation in 0.6 – 1.6 keV, as functions of the timescales.

edge depth becomes shallower, as the source brightens and the warm absorber gets more highly ionized. This is consistent with what was observed with ASCA (Otani et al. 1996). Invariable OVII depth regardless of the flux variation, which was also observed with ASCA (Otani et al. 1996), suggests that the OVII edge originates from a rather extended area in the line of sight, so that the OVII edge depth does not respond to the flux variation instantaneously. The point here is that the spectral variation below 1.6 keV can be reproduced by sole variation of the photoionization as a natural consequence of the intrinsic flux changes, while the photon index is invariable.

4. Discussion

We studied spectral variation of MCG-6-30-15 observed with Suzaku in 2006 January, and found a clear correlation between the 6 – 10 keV flux and the spectral ratio of 0.5 – 3.0 keV/6.0 – 10 keV (Figure 4). Amplitude of the flux variation and the accompanying spectral change increases when the variation timescales become longer from 5 ksec to 200 ksec (Figure 5). We fitted the 1 – 40 keV energy

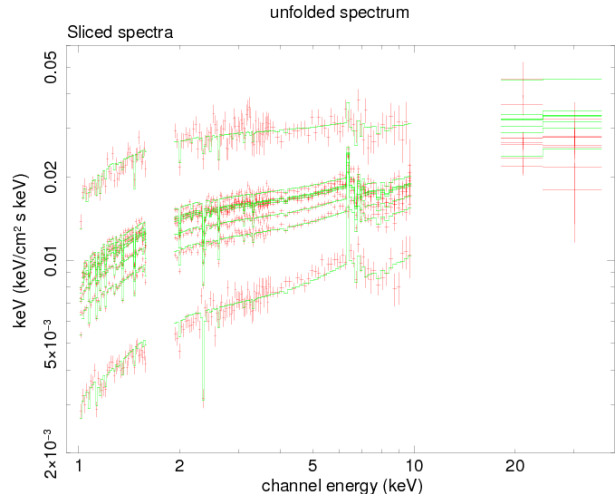


Fig. 9. Unfolded energy spectra for the eight intensity-sliced spectra calculated from the model only varying the power-law normalization and ionization degree of the lower-ionized warm absorber.

spectra with the spectral model including a cut-off power-law, two warm absorbers and neutral reflection (Figure 1). The observed spectral variation was almost equally explained by variation of either photon index of the direct component, ionization degree of the lower-ionized warm absorber, or column density of the warm absorber, whereas the neutral reflection component was invariable throughout the observation. We could not clearly judge if the intrinsic photon index or warm absorber parameters are variable, but it is most physically reasonable to assume that the photoionization degree increases with increasing intensities. We also fit the eight intensity-sliced spectra with the model varying the power-law normalization and the ionization parameter (Table 4). In Fig.9, we show the incident spectral changes for the intensity sliced spectra calculated from the best-fit parameters.

In the top panel of Fig.10, we show relation between the variation timescales and ionization degrees of the low-ionized warm absorber. Also, in the middle panel of Fig.10, we show the relations between the variation time scales and the power-law normalizations. It is obvious that both the ionization degree and the power-law normalization for the bright state increases with the variation time-scale, while those for the faint state decreases with the variation time-scale. In the bottom panel of Fig. 10, we show relation between the power-law normalization and the ionization degree of the lower-ionized warm absorber, which indicates a clear correlation as $\log \xi = (1.7 \pm 0.2) \times \log K + (4.7 \pm 0.3)$.

Spectral variation in 0.6 – 1.6 keV can be also explained by change of the OVIII edge depth due to photoionization (Figure 8). Therefore, we suggest that spectral variation of MCG-6-30-15 in 0.6 keV to 40 keV on timescales of 5 ksec to 200 ksec is primarily explained by change of the ionization degree of warm absorbers due to photoionization, while power-law photon-index and the disk reflection

Table 2. Results of spectral fitting in 1–40 keV for the “bright” and “faint” spectra. *

timescale	5 ksec		9 ksec		15 ksec		40 ksec		75ksec		200 ksec	
state	bright	faint	bright	faint	bright	faint	bright	faint	bright	faint	bright	faint
<i>Model 1: power-law normalization and its index are variable</i>												
N_H (10^{21} cm^{-2})							1.7±0.1					
N_H (10^{22} cm^{-2})							10±2					
log ξ							3.56±0.05					
N_H (10^{21} cm^{-2})							1.4±0.2					
log ξ							1.03 ^{+0.03} _{-0.11}					
Line E (keV)							6.35 (fix)					
sigma (keV)							0.01 (fix)					
norm (10^{-5})							1.7±0.1					
EW (eV)	35±2	41±3	35±2	42±3	34±2	42±3	33±2	44±3	31±2	44±3	30±2	44±3
cutoffpl K (10^{-2})	1.51 ^{+0.01} _{-0.02}	1.26 ^{+0.01} _{-0.02}	1.57 ^{+0.01} _{-0.02}	1.22 ^{+0.01} _{-0.02}	1.64 ^{+0.01} _{-0.02}	1.18 ^{+0.01} _{-0.02}	1.72 ^{+0.01} _{-0.02}	1.11 ^{+0.01} _{-0.02}	1.83 ^{+0.01} _{-0.03}	1.13 ^{+0.01} _{-0.02}	1.95±0.02	1.10 ^{+0.01} _{-0.02}
photon index	1.91±0.01	1.90±0.01	1.91±0.01	1.89±0.01	1.92±0.01	1.88±0.01	1.93±0.01	1.88±0.01	1.94±0.01	1.88±0.01	1.95±0.01	1.87±0.01
E_{cut} (keV)							160 (fix)					
cosIncl							0.866 (fix)					
pextrav K (10^{-2})							1.07±0.08					
Line E (keV)							2.35±0.01					
sigma (keV)							0.01 (fix)					
norm (10^{-5})							-2.12±0.22					
reduced chisq (d.o.f)							1.30 (2786)					
<i>Model 2: power-law normalization and ionization degree of the lower-ionized warm absorber are variable</i>												
N_H (10^{21} cm^{-2})							2.14±0.05					
N_H (10^{22} cm^{-2})							3.2 ^{+0.8} _{-0.6}					
log ξ							3.29±0.04					
N_H (10^{21} cm^{-2})							2.5±0.3					
log ξ	1.57±0.05	1.56 ^{+0.05} _{-0.06}	1.60±0.05	1.53 ^{+0.05} _{-0.06}	1.67±0.05	1.46 ^{+0.05} _{-0.09}	1.74 ^{+0.05} _{-0.06}	1.41±0.06	1.80 ^{+0.05} _{-0.06}	1.43±0.06	1.86 ^{+0.07} _{-0.06}	1.39 ^{+0.05} _{-0.06}
Line E (keV)							6.35 (fix)					
sigma (keV)							0.01 (fix)					
norm (10^{-5})							1.7±0.1					
EW (eV)	36±2	42±3	35±2	43±3	34±2	43±3	33±2	45±3	31±2	45±3	30±2	46±3
cutoffpl K (10^{-2})	1.64±0.02	1.37±0.02	1.68 ^{+0.02} _{-0.01}	1.33±0.02	1.73±0.02	1.31±0.02	1.79±0.02	1.25±0.01	1.90±0.02	1.26±0.01	2.00±0.02	1.24±0.01
photon index							1.96±0.01					
E_{cut} (keV)							160 (fix)					
cosIncl							0.866 (fix)					
pextrav K (10^{-2})							1.7±0.1					
Line E (keV)							2.35±0.01					
sigma (keV)							0.01 (fix)					
norm (10^{-5})							-2.3±0.2					
reduced chisq (d.o.f)							1.41 (2787)					
<i>Model 3: power-law normalization and column density of the lower-ionized warm absorber are variable</i>												
N_H (10^{21} cm^{-2})							2.2±0.1					
N_H (10^{22} cm^{-2})							3.0±0.7					
log ξ							3.28±0.04					
N_H (10^{21} cm^{-2})	2.8±0.4	3.0±0.4	2.5±0.4	3.2±0.4	2.1±0.4	3.7±0.4	1.8±0.3	4.0±0.5	1.4±0.4	3.9 ^{+0.5} _{-0.4}	1.1±0.3	4.2 ^{+0.5} _{-0.4}
log ξ							1.73±0.05					
Line E (keV)							6.35 (fix)					
sigma (keV)							0.01 (fix)					
norm (10^{-5})							1.7±0.1					
EW (eV)	36±2	42±3	35±2	43±3	34±2	43±3	33±2	45±3	32±2	45±3	30±2	46±3
cutoffpl K (10^{-2})	1.63 ^{+0.03} _{-0.02}	1.37±0.02	1.67 ^{+0.03} _{-0.02}	1.33±0.02	1.71 ^{+0.03} _{-0.02}	1.31±0.02	1.77 ^{+0.03} _{-0.02}	1.25±0.02	1.87 ^{+0.03} _{-0.02}	1.26 ^{+0.02} _{-0.01}	1.96 ^{+0.03} _{-0.02}	1.24±0.02
photon index							1.96±0.01					
E_{cut} (keV)							160 (fix)					
cosIncl							0.866 (fix)					
pextrav K (10^{-2})							1.56±0.01					
Line E (keV)							2.35±0.01					
sigma (keV)							0.01 (fix)					
norm (10^{-5})							-2.26±0.23					
reduced chisq (d.o.f)							1.35 (2787)					

* See the footnote of Table 1.

Table 3. Table 3. Results of spectral fitting in 0.6–1.6 keV for the “bright” and “faint” spectra. *

timescale	5 ksec		9 ksec		15 ksec		40 ksec		75 ksec		200 ksec	
state	bright	faint	bright	faint	bright	faint	bright	faint	bright	faint	bright	faint
photon index	1.82±0.05											
K (10^{-2})	1.28±0.01	1.06±0.01	1.31±0.01	1.03±0.01	1.37±0.01	1.00±0.01	1.43±0.01	0.95±0.01	1.52±0.01	0.96±0.01	1.60±0.01	0.94±0.01
edge E (keV)	0.706±0.001											
MaxTau	0.67±0.01											
edge E (keV)	0.855±0.002											
MaxTau	0.34±0.02	0.31±0.02	0.33±0.02	0.32±0.02	0.33±0.02	0.32±0.02	0.31±0.02	0.34±0.02	0.32±0.02	0.35±0.02	0.30±0.02	0.34±0.02
reduced chisq (d.o.f)	1.30 (1604)											

* Errors are quoted at statistical 90% level.

Table 4. Results of spectral fitting in 1–40 keV for the intensity sliced spectra when only the power-law normalization and the ionization degree of the lower-ionized absorber are varied. *

state	slice 1	slice 2	slice 3	slice 4	slice 5	slice 6	slice 7	slice 8
N_H (10^{21} cm^{-2})					2.3±0.1			
N_H (10^{22} cm^{-2})					3.3±0.9			
log ξ					3.27 ^{+0.04} _{-0.06}			
N_H (10^{21} cm^{-2})					4.1±0.3			
log ξ	1.24 ^{+0.12} _{-0.10}	1.57±0.06	1.69 ^{+0.06} _{-0.03}	1.70±0.06	1.74 ^{+0.05} _{-0.06}	1.86 ^{+0.05} _{-0.06}	1.75±0.06	2.05±0.12
Line E (keV)					6.35 (fix)			
sigma (keV)					0.01 (fix)			
norm (10^{-5})					1.7±0.2			
EW (eV)	68±6	44±4	40±4	36±3	36±3	35±3	33±3	21±2
cutoffpl K (10^{-2})	0.75±0.02	1.35±0.03	1.54±0.04	1.72±0.04	1.75±0.04	1.77±0.04	1.89±0.05	3.23±0.12
photon index					2.04±0.02			
E_{cut} (keV)					160 (fix)			
cosIncl					0.866 (fix)			
pexrav K (10^{-2})					2.8 ^{+0.5} _{-0.3}			
Line E (keV)					2.35±0.01			
sigma (keV)					0.01 (fix)			
norm (10^{-5})					-2.4±0.3			
reduced chisq (d.o.f)					1.24 (1143)			

* See the footnote of Table 1.

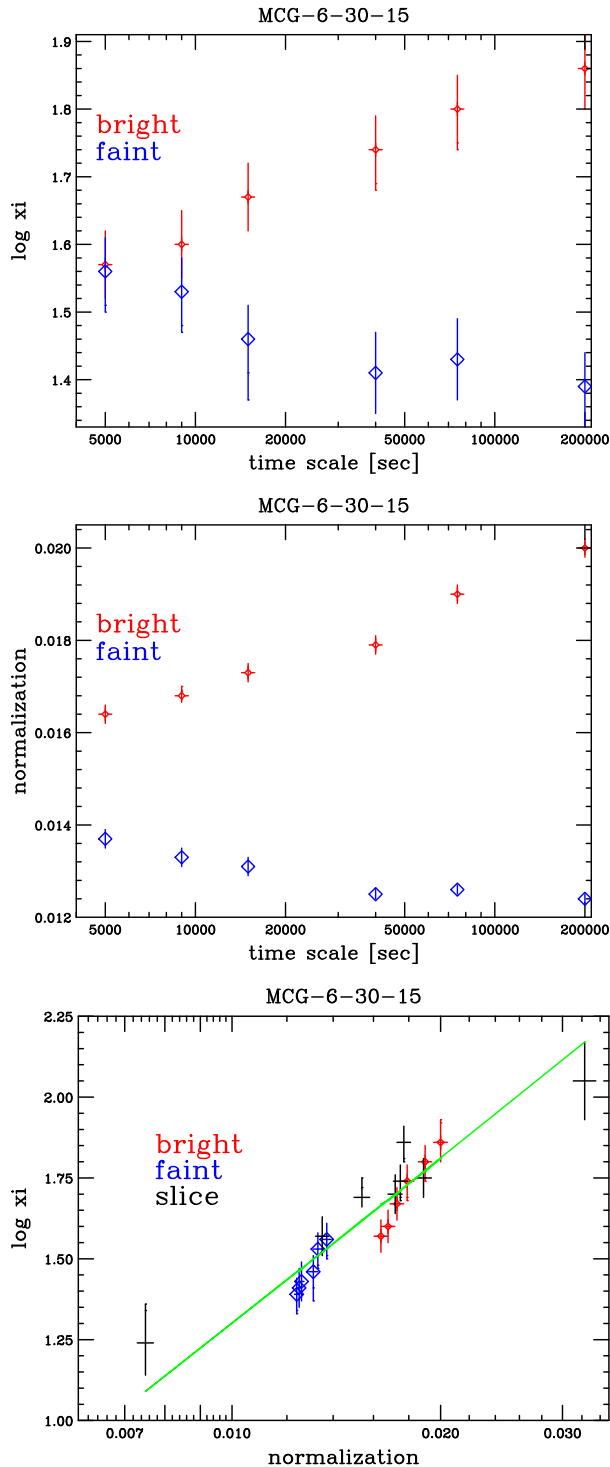


Fig. 10. Top: Relation between the variation time scale and ionization degree for the bright and faint spectra. Middle: Relation between the variation time scale and power-law normalization for the bright and faint spectra. Bottom: Relation between the ionization degree and power-law normalization for the bright, faint and sliced spectra.

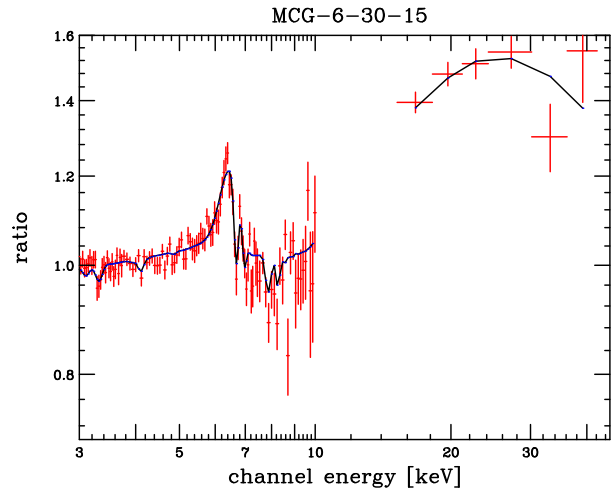


Fig. 11. Ratio of our best-fit model (black) and the observed data (red) to a power-law function. The power-law slope is determined using the data only in 3.0–4.0 keV and 7.5–12 keV. Note that our model includes a moderately broad iron emission line at 6.42 keV ($1\sigma = 290$ eV), but not an extremely distorted one with relativistic effects.

component are invariable.

Note that our model does not include an extremely broad iron emission line. If the intrinsic line width is allowed to be free, the central line energy is 6.42 ± 0.06 keV, and the intrinsic line width is $1\sigma = 290 \pm 60$ eV (Figure 2). With the combination of the cold reflection, mildly broad emission line and warm absorber, our model can successfully fit the seemingly broad iron line feature (Figure 2). In Figure 11, we show a ratio of our best-fit model to a power-law function, as well as a ratio of the observed spectrum to the same power-law function. The broad-line like structure down to ~ 4 keV is recognized both in the model and data, but this is naturally explained by combination of the disk reflection, warm absorber and a mildly broad gaussian line that is not significantly redshifted. We conclude that an extremely broad emission line is not required if multiple warm absorbers are taken into account, which agrees with Miller et al. (2008), while our model is simpler.

Also we point out that normalization of the reflection component requires $\Omega/2\pi \sim 1$ in our model, not > 3 as Miniutti et al. (2007) advocates. Difference is mainly due to the fact that we included warm absorbers, and used neutral reflection without relativistic smearing. So that the constancy of the reflection component is explained by the light-bending model, all the disk reflection *must* take place within $3 r_g$, in which case the reflection normalization requires $\Omega/2\pi \sim 3$ (Miniutti & Fabian 2004). On the other hand, our result favors a smaller solid angle of the reflector. Also, invariability of the neutral reflection component suggests that the reflection takes place far enough from the black hole, so that the intrinsic variation is smeared. If that is true, we would expect a narrow line of the equivalent width ~ 150 eV (e.g., George and Fabian 1991) for $\Omega/2\pi \sim 1$, much larger than the observed value

(~ 18 eV; Young et al. 2005). If we allow the line width free, we obtain the equivalent width ~ 110 eV (table 1), which may be reconciled with the reflector having $\Omega/2\pi \sim 1$. In this case, we require a mechanism to mildly broaden the line width up to $1\sigma \approx 290$ eV. If this intrinsic line width is from Keplerian motion, with $v/c \sim 0.29/6.35$, v is $\sim 14,000$ km/s, which does not seem too infeasible to be material on the innermost edge of the broad line region.

In summary, we found a characteristic spectral variation of MCG-6-30-15, that is explained by variation of ionization degree of the warm absorber accompanying the flux variation, while the neutral reflection component was invariable throughout the observation. Considering the warm absorber, the observed energy spectrum is explained by a mildly broadened iron line, which is not significantly red-shifted, and a neutral and constant disk reflection component of which solid angle is $\Omega/2\pi \sim 1$. Still, there needs a mechanism to keep the reflection component constant while direct component is variable.

5. Acknowledgement

The authors would like to thank the referee, Prof. Chris Done, for her valuable suggestions and comments. This research has made use of public data obtained through the Data ARchives and Transmission System (DARTS), provided by the Institute of Space and Astronautical Science (ISAS), Japan Aerospace Exploration Agency (JAXA). For data reduction, we used the software provided by the High Energy Astrophysics Science Archive Research Center (HEASARC) at NASA/Goddard Space Flight Center. T.M. acknowledges Japan Society for the Promotion of Science (JSPS) for financial supports via the Research Fellowship for Young Scientists.

Appendix 1. Note Added in the Proof

After the paper was submitted, the referee pointed out availability of the XSTAR 2.1ln11, and requested to mention effects of the XSTAR version differences. XSTAR 2.1kn8, which is used throughout the paper, does not have all the new K edge structures of Kallman et al. (2004). These are only incorporated in versions 2.1ln and above. This makes little difference at high ionisation, but does put considerably more absorption structures in the K-edge at low absorptions.

We report a result using XSTAR 2.1ln11, where we fitted the time-averaged spectra 1–40 keV with a broad emission line ($\chi^2/\text{d.o.f} = 277.2/222$). We got parameters which agree with those in Table 1 (left) within 90 % errors besides the following parameters: N_H of the neutral absorber is $(1.4 \pm 0.3) \times 10^{21} \text{cm}^{-2}$ that of higher ionized warm absorber is $(23 \pm 13) \times 10^{22} \text{cm}^{-2}$, and that of lower-ionized warm absorber is $(4.1 \pm 1.1) \times 10^{21} \text{cm}^{-2}$.

In summary, conclusion of our paper is unchanged due to recent version change of XSTAR.

References

- Anders, E. & Ebihara, M. 1982, *Geochim Cosmochim Acta*, 46, 2363
- Arnaud, K. 1996, *Astronomical Data Analysis Software and Systems V*, A.S.P., Conference Series, 101, 17
- Boldt, E. 1987, *Observational Cosmology*, 124, 611
- Balucinska-Church, M., & McCammon, D. 1992, *ApJ*, 400, 699
- de Rosa, A., Piro, L., Perola, G.C., Capalbi, M., Cappi, M., Grandi, P., Maraschi, L., and Petrucci, P.O., 2007, *A&A*, 463, 903
- Fabian, A. C., et al. 2002, *MNRAS*, 335, L1
- Fabian, A. C., Rees, M. J., Stella, L., & White, N. E. 1989, *MNRAS*, 238, 729
- Fisher, K. B., Huchra, J. P., Strauss, M. A., Davis, M., Yahil, A., & Schlegel, D. 1995, *ApJS*, 100, 69
- George, I. M. & Fabian, A. C. 1991, *MNRAS*, 249, 352
- Gibson, R. R., Canizares, C. R., Marshall, H. L., Young, A. J., Lee, J. C. 2007, *ApJ*, 655, 749
- Grevesse, N., Noels, A., and Sauval, A. 1996, in “Cosmic Abundances” ASP Conference Series, 99, S. Holt and G. Sonneborn, eds.
- Guainazzi, M., et al. 1999, *A&A*, 341, L27
- Inoue, H., & Matsumoto, C. 2003, *PASJ*, 55, 625
- Ishida, M., Suzuki, K., & Someya, K. 2007, *JX-ISAS-SUZAKU-MEMO-2007-11*, 1
- Iwasawa, K., et al. 1996, *MNRAS*, 282, 1038
- Kallman, T. R., Palmeri, P., Bautista, M. A., Mendoza, C., & Krolik, J. H. 2004, *ApJS*, 155, 675
- Koyama, K., et al. 2007, *PASJ*, 59, S23
- Lee, J. C., Fabian, A. C., Brandt, W. N., Reynolds, C. S., & Iwasawa, K. 1999, *MNRAS*, 310, 973
- Lee, J. C., et al. 2001, *ApJ*, 554, L13
- Magdziarz, P., & Zdziarski, A. A. 1995, *MNRAS*, 273, 837
- Matsumoto, C., Inoue, H., Fabian, A. C., & Iwasawa, K. 2003, *PASJ*, 55, 615
- Miller, L., Turner, L. J. & Reeves, J. N. 2008, *A&A*, 483, 437
- Miniutti, G., & Fabian, A. C. 2004, *MNRAS*, 349, 1435
- Miniutti, G., et al. 2007, *PASJ*, 59, 315
- Mitsuda, K., et al. 2007, *PASJ*, 48, 211
- Niedźwiecki, A., & Życki, P. T. 2008, *MNRAS*, 386, 759
- Ogawara, Y., Doi, K., Matsuoka, M., Miyamoto, S., & Oda, M. 1977, *Nature*, 270, 154
- Ogle, P.M, Marshall, H.L, Lee, J.C., and Canizares, C.R., 2000, *ApJ*, 545, L81
- Osterbrock, T., et al. 1996, *A&A*, 309, 781
- Otani, C., et al. 1996 *PASJ*, 48, 211O
- Ponti, G., Cappi, M., Dadina, M., & Malaguti, G. 2004, *A&A*, 417, 451
- Reynolds, C. S., Fabian, A. C., Nandra, K., Inoue, H., Kunieda, H., & Iwasawa, K. 1995, *MNRAS*, 277, 901
- Sako, M., et al. 2003, *ApJ*, 596, 114
- Shull, J. M., & van Steenberg M. 1982, *ApJS*, 48, 95
- Takahashi, K., Inoue, H., & Dotani, T. 2002, *PASJ*, 54, 373
- Takahashi, T., et al. 2007, *PASJ*, 59, S35
- Tanaka, Y., et al. 1995, *Nature*, 375, 659
- Turner, A. K., Fabian, A. C., Vaughan, S., & Lee, J. C. 2003, *MNRAS*, 346, 833
- Turner, A. K., Fabian, A. C., Lee, J. C., & Vaughan, S. 2004, *MNRAS*, 353, 319
- Vaughan, S., & Edelson, R. 2001, *ApJ*, 548, 694
- Vaughan, S., & Fabian, A. C. 2004, *MNRAS*, 348, 1415
- Young, A. J., Lee, J. C., Fabian, A. C., Reynolds, C. S., Gibson, R. R., & Canizares, C. R. 2005, *ApJ*, 631, 733